

PHASE-DEPENDENT EXCITONIC LIGHT HARVESTING AND PHOTOVOLTAIC LIMITS IN MONOLAYER Y_2TeO_2 MOENES

AN ARXIV PREPRINT

 **Bill D. A. Huacarpuma**¹,  **José A. dos S. Laranjeira**²,  **Nicolas F. Martins**²,  **Julio R. Sambrano**²,
 **Kleuton A. L. Lima**³,  **Santosh K. Tiwari**⁴,  **Alexandre C. Dias**¹, and  **Luiz A. Ribeiro Jr**^{1,†}

¹Computational Materials Laboratory, LCCMat, Institute of Physics, University of Brasília, 70910-900, Brasília, Federal District, Brazil

²Modeling and Molecular Simulation Group, São Paulo State University (UNESP), School of Sciences, Bauru 17033-360, SP, Brazil

³Department of Applied Physics and Center for Computational Engineering and Sciences, State University of Campinas, Campinas, 13083-859, SP, Brazil

⁴Centre for New Materials and Surface Engineering, Department of Chemistry, NMAM Institute of Technology (NMAMIT), Nitte (Deemed to be University), Nitte 574110, Karnataka, India

  *bdaparicioh@gmail.com
  †ribeirojr@unb.br

February 26, 2026

ABSTRACT

We investigate phase-dependent electronic and excitonic phenomena in monolayer Y_2TeO_2 MOenes in the 1T and 2H polymorphs using first-principles theory and an effective many-body framework. Phonon spectra and elastic stability criteria establish both phases as dynamically and mechanically stable. Quasiparticle band structures reveal direct gaps in the near-infrared to visible range, with gap values increasing systematically from semilocal to hybrid exchange treatments. Optical spectra computed using a tight-binding Bethe-Salpeter approach demonstrate pronounced excitonic resonances arising from reduced dimensionality and weak dielectric screening. The exciton binding energies reach 152 meV in the 1T phase and 126 meV in the 2H phase, reflecting enhanced quantum confinement in the structurally denser phase. Our results identify Y_2TeO_2 monolayers as a rare class of stable, direct-gap MOenes with strong excitonic effects, providing a platform for exploring many-body physics in low-dimensional oxychalcogenide systems especially for photovoltaic applications.

Keywords MOenes · Y_2TeO_2 monolayers · Excitonic effects · Bethe–Salpeter equation · Photovoltaic efficiency

1 Introduction

The discovery of two-dimensional (2D) transition-metal carbides in 2011 marked a major milestone in materials science and led to the development of MXenes and related families such as MBenes [1, 2]. MXenes are typically produced by selectively removing the A-layer (e.g., Al, Si) from layered ternary precursors known as MAX phases, such as Ti_3AlC_2 , Ti_3SiC_2 and others [3]. This chemical exfoliation process yields atomically thin sheets like Ti_3C_2 [4]. The general formula of MXenes is $M_{n+1}X_nT_x$ ($n = 1, 2, 3 \dots$) [3], where M is an early transition metal, X is carbon and/or nitrogen, and T_x represents surface terminations introduced during synthesis. Several etching strategies have been developed to remove the A-layer and tailor the surface chemistry [5]. Most conventional methods employ

fluorine-containing etchants such as HF [6], LiF/HCl mixtures [7], bifluoride salts [8, 9], or fluorinated molten salts [10]. These approaches efficiently extract the A-layer and commonly result in $-O$, $-OH$, and $-F$ surface groups [11]. For instance, Kajiyama *et al.* [12] demonstrated that LiF/HCl etching enhances electrochemical energy storage compared to direct HF treatment, partly due to increased interlayer spacing associated with $-Cl$ species. However, $-F$, $-O$, and $-OH$ groups remain dominant surface terminations. The presence and quantification of hydroxyl groups are still debated because hydrogen-related signals are difficult to detect experimentally [13]. To address excessive fluorine content, post-synthesis alkaline treatments using NaOH, TBAOH etc. have been proposed to partially replace halogen terminations with O/OH groups, thereby improving surface reactivity and chemical stability [14, 15].

Surface terminations strongly influence the electronic properties of MXenes. Depending on composition and functionalization, MXenes can exhibit metallic, half-metallic, semiconducting, or even topologically nontrivial behavior [16]. But, intrinsically semiconducting MXenes are relatively rare. Only a few systems, such as Mo_2CT_x [17], and $Mo_2TiC_2T_x$ [18], have been realized experimentally and tested for various applications [19]. In the same line, many others have been predicted theoretically, including M_2CO_2 ($M = Ti, Zr, Hf, Mn, W$) [20], $2D Y_2CT_xI$ ($T_x = Br, Cl, F, H$) [21], $MM'CT_2$ ($M = Sc; M' = Y; T = Br, Cl, F, H, I, O, OH, S, Se, Te$) [22], $Cr_2TiC_2T_2$ ($T = F, OH$) [23], M_2CF_2 ($M = Cr, Mo$) [24], $NbScCO_2$ [25], and M_2CT_2 ($M = Sc, Y; T = O, F, OH$) [26]. The limited availability of stable semiconducting MXenes motivates the exploration of alternative 2D materials with tunable band gaps and robust structural stability.

In this direction, MXene-like metal-oxide monolayers, referred to as MOenes, have emerged as promising candidates [27]. The prototype 1T-Ti₂O monolayer has been reported as a high-performance anode material and as a superconductor, while its fluorinated derivative 1T-Ti₂OF₂ exhibits a direct semiconducting band gap [28]. Recent synthesis advances, including molten-salt electrochemical routes and thin-film growth on α -Al₂O₃ substrates, indicate that MOenes are experimentally feasible and structurally stable [29, 30]. The oxide-based framework of MOenes also offers improved chemical robustness compared to carbide and nitride counterparts. Notably, MOenes show considerable potential across energy and electronic applications. For instance, Wan *et al.* [31] reported that Ti₂OX₂ ($X = F, Cl$) monolayers exhibit strong thermoelectric performance, combining high Seebeck coefficients with good electrical conductivity and low lattice thermal conductivity. Qiu *et al.* [32] demonstrated that MOenes and their Janus structures possess enhanced piezoelectric responses compared to conventional 2D materials such as 2H-MoS₂, with Ti₂OH₂ showing an in-plane coefficient of 6.09 pm/V. In addition, Bolen *et al.* [33] found that Mo₂ScC₂O₂ combines a high Young's modulus with low thermal conductivity, suggesting applications in mechanical sensing and thermal management.

Motivated by aforesaid developments, we investigate Y₂TeO₂ MOene monolayers in both 1T and 2H phases. Structural stability is evaluated using phonon dispersion, elastic constants, and *ab initio* molecular dynamics simulations. Electronic properties are examined through band structure and density of states analyses to determine band-gap characteristics and carrier behavior. Optical properties, including absorption coefficient, refractive index, and reflectivity, are calculated within the independent-particle framework and with electron-hole interactions included via the Bethe-Salpeter equation. Excitonic binding energies are extracted to assess many-body effects relevant for optoelectronic applications. Finally, the photovoltaic potential is estimated using the spectroscopic limited maximum efficiency and Shockley-Queisser approaches, yielding predicted power conversion efficiencies between 30.56% and 32.66%. These results highlight Y₂TeO₂ MOene as a promising 2D semiconductor for next-generation optoelectronic and energy-harvesting devices.

2 Methodology

First-principles simulations were performed within the framework of density functional theory (DFT) [34, 35] using the Vienna *Ab initio* Simulation Package (VASP, version 6.5.0) [36, 37]. The exchange-correlation energy was treated using the Perdew-Burke-Ernzerhof (PBE) generalized gradient approximation [38], in combination with the projector augmented-wave (PAW) method [39, 40]. A plane-wave kinetic energy cutoff of 700 eV was employed to ensure total-energy convergence.

Brillouin-zone integrations were carried out using Monkhorst–Pack \mathbf{k} -point meshes of $12 \times 12 \times 1$ for structural relaxations and $36 \times 36 \times 1$ for electronic structure calculations. The electronic self-consistency criterion was set to $1e^{-6}$ eV. Geometry optimizations were performed until the residual forces on each atom were smaller than 0.01 eV/Å. A vacuum spacing of 23 Å was introduced along the out-of-plane direction to eliminate spurious interactions between periodic images of the Y_2TeO_2 -1T and Y_2TeO_2 -2H monolayers. To obtain accurate band-gap values, electronic band structures were additionally calculated using the screened hybrid Heyd–Scuseria–Ernzerhof (HSE06) functional [41, 42].

We used the Phonopy package to perform phonon dispersion calculations to assess the system’s dynamical stability [43]. These computations were executed using density functional perturbation theory (DFPT) with a $2 \times 2 \times 1$ supercell and a $6 \times 6 \times 1$ \mathbf{k} -point mesh. We used the Wannier90 code [44] to generate maximally localized Wannier functions (MLWFs) from a tight-binding (TB) Hamiltonian derived from HSE06 electronic structure calculations.

The WanTiBEXOS code [45] was used to figure out the optical and excitonic properties. The Wannier basis comprised d -orbital projections for Y atoms, p orbitals for Te atoms, and s and p orbitals for O atoms. We examined optical responses in both the independent-particle approximation (IPA), which does not account for electron-hole interactions, and the Bethe-Salpeter equation (BSE) formalism, which does. For these calculations, a 2D \mathbf{k} -point density of $120/\text{Å}$ was used. To accurately characterize reduced-dimensional screening effects, BSE calculations employed a two-dimensional truncated Coulomb potential (V2DT) [46]. The dielectric function was calculated using a Gaussian smearing of 0.05 eV, with five conduction bands ($n_c = 5$) and four valence bands ($n_v = 4$) to capture low-energy optical and excitonic features accurately. A schematic representation of the parameters and computational tool simulation protocol is shown in Figure 1.

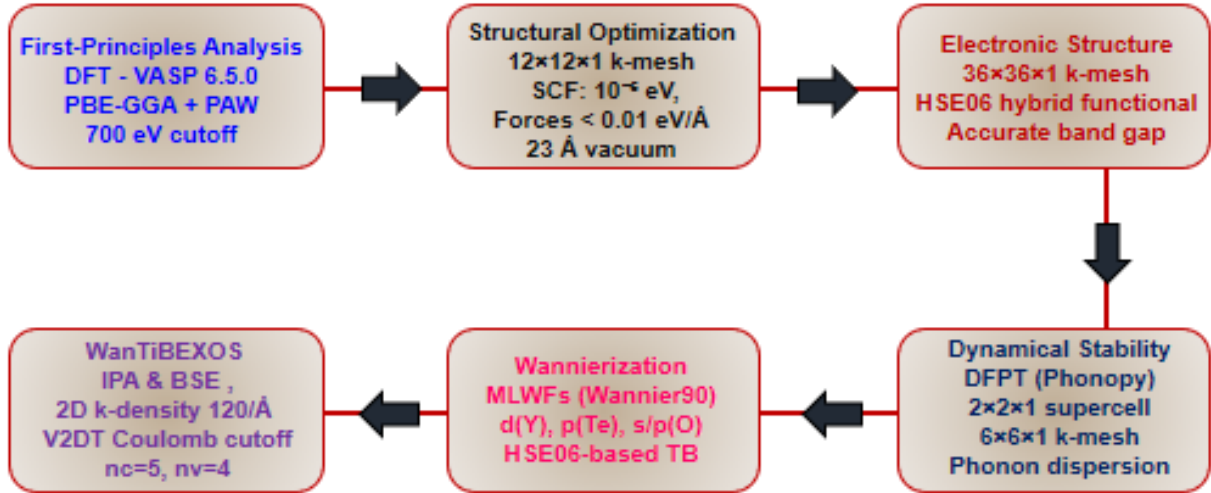


Figure 1: Block diagram steps and computational tools employed for the investigated 1T and 2H Y_2TeO_2 monolayers.

3 Results

3.1 Structural and mechanical properties

Figure 2 shows the top and side views of the optimized atomic structures of the Y_2TeO_2 monolayers in the 1T and 2H phases. Both phases have a hexagonal lattice. The 1T phase belongs to the $P\bar{3}m1$ (No. 164) space group, and the 2H phase crystallizes in the $P\bar{6}m2$ (No. 187) symmetry. In both cases, the Y atoms create a close-packed hexagonal sublattice. The Te and O atoms, on the other hand, are in different coordination environments above and below the Y plane. This creates a layered metal-oxide framework that is typical of MOenes.

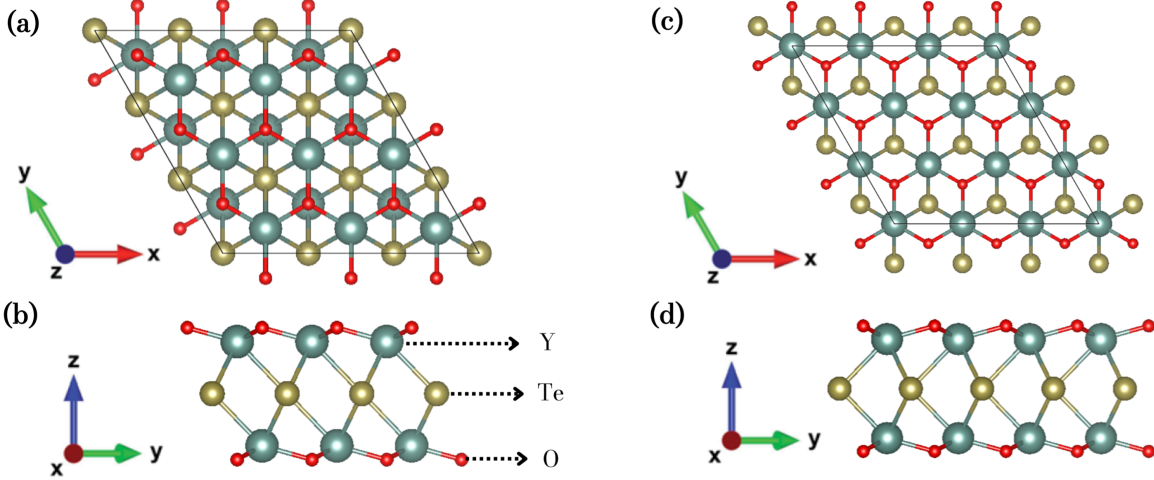


Figure 2: Structural models of the Y_2TeO_2 monolayers. Panels (a) and (b) show the top and side views of the Y_2TeO_2 -1T phase, while panels (c) and (d) display the corresponding views for the Y_2TeO_2 -2H phase. Y, Te, and O atoms are represented by golden-brown, silver-green, and red spheres, respectively.

Table 1 shows the lattice parameters, interaxial angles (α , β , and γ), monolayer thicknesses, and cohesive energies that were found after complete structural relaxation at the PBE level. The in-plane lattice constants for the two phases are almost the same: $a_0 = 3.744 \text{ \AA}$ for Y_2TeO_2 -1T and $a_0 = 3.745 \text{ \AA}$ for Y_2TeO_2 -2H. This shows that changing the stacking order doesn't have a significant effect on the in-plane bonding network. These values align with earlier theoretical studies of analogous Y-based MOene systems, exhibiting deviations of $< 1\%$ [23], attributable to variations in exchange-correlation functionals and structural relaxation methodologies.

Table 1: Optimized structural parameters and energetic stability of the Y_2TeO_2 monolayers in the 1T and 2H phases. The table lists the in-plane lattice constant (a_0), interaxial angles (α , β , and γ), monolayer thickness including a van der Waals length correction of 3.31 \AA (t_0), and the cohesive energy per atom (E_{coh}) calculated at the PBE level.

System	a_0 (\AA)	$\alpha = \beta \neq \gamma$	t_0 (\AA)	E_{coh} (eV/atom)
Y_2TeO_2 -1T	3.744	$90=90 \neq 120$	9.00	-6.021
Y_2TeO_2 -2H	3.745	$90=90 \neq 120$	8.99	-6.029

We calculated the cohesive energies of the proposed monolayers to assess their energetic stability.

$$E_{\text{coh}} = \frac{E_{\text{tot}}(\text{Y}_2\text{TeO}_2) - \sum_{i=\text{Y,Te,O}} N_i E_i}{N_{\text{atoms}}}, \quad (1)$$

where $E_{\text{tot}}(\text{Y}_2\text{TeO}_2)$ is the total energy of the monolayer, N_i and E_i are the number and isolated-atom energy of species i (Y, Te, and O), and N_{atoms} is the total number of atoms in the unit cell. The cohesive energies of -6.021 eV/atom for the 1T phase and -6.029 eV/atom for the 2H phase show that the atoms are strongly bonded to each other and that the formation is thermodynamically favorable. These values are similar to those found for other stable 2D metal-oxide and MXene-derived systems [28, 29], which shows that both Y_2TeO_2 polymorphs are intrinsically stable in terms of energy.

We used phonon-dispersion calculations to assess the dynamic stability of Y_2TeO_2 monolayers in the 1T and 2H phases. You can see the results in Fig. 3(a) and (c). In both instances, all phonon branches display positive frequencies across the entire Brillouin zone, with no imaginary modes observed. This behavior clearly indicates that both polymorphs are dynamically stable at zero temperature and that no structural instabilities arise from lattice distortions. The overall

phonon spectrum shows that the acoustic and optical branches are well separated. This is a common feature in stable two-dimensional metal-oxide and MXene-derived systems.

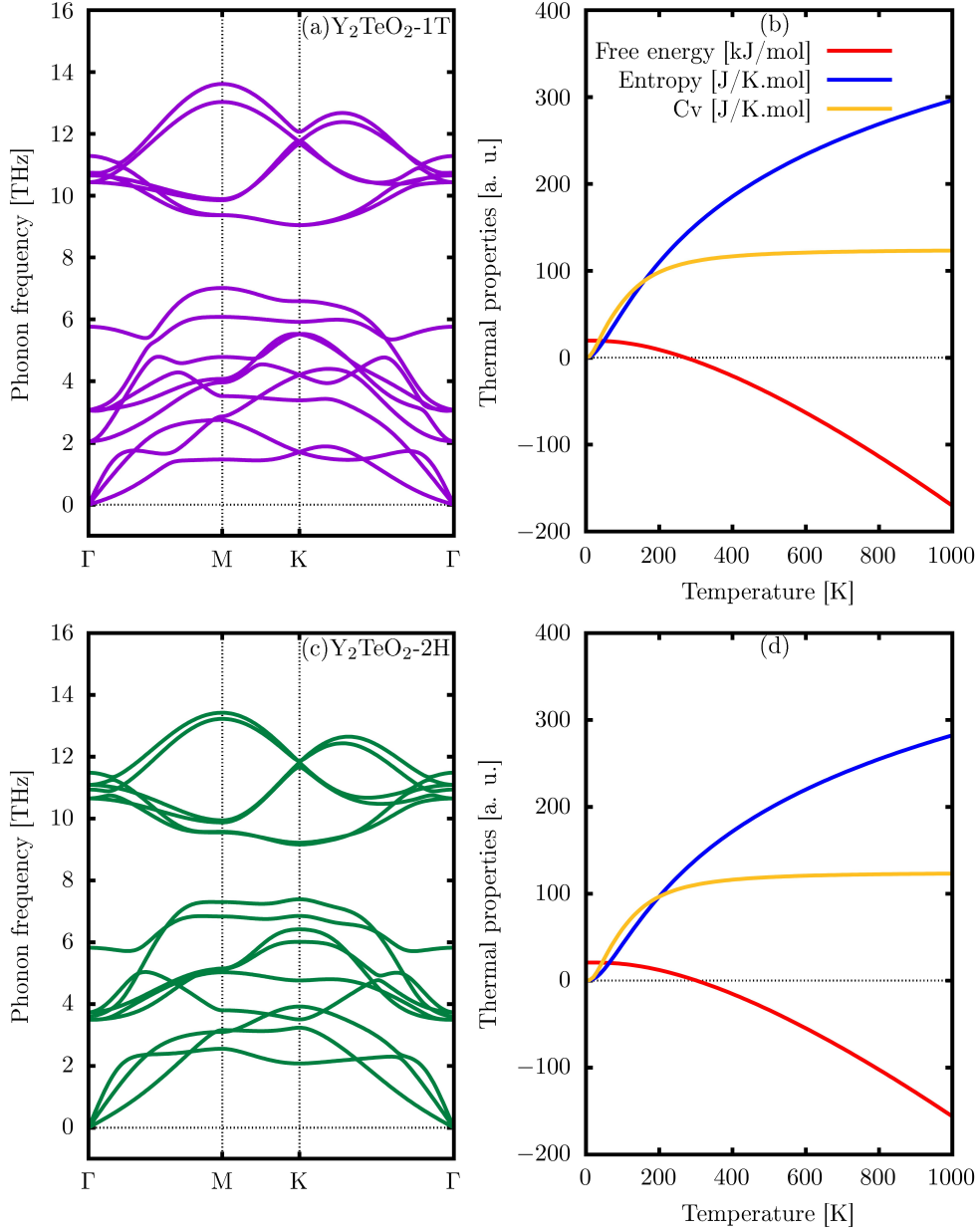


Figure 3: Phonon dispersion relations and thermodynamic properties of the Y_2TeO_2 monolayers. Panels (a) and (c) show the phonon dispersion curves of the Y_2TeO_2 -1T and Y_2TeO_2 -2H phases, respectively, calculated at the PBE level. Panels (b) and (d) display the temperature dependence of the Helmholtz free energy $F(T)$, entropy $S(T)$, and heat capacity at constant volume $C_v(T)$ for the corresponding monolayers.

In addition to dynamic stability, the phonon density of states was used to find critical thermodynamic quantities like the Helmholtz free energy $F(T)$, entropy $S(T)$, and heat capacity at constant volume $C_v(T)$. These quantities are shown in Fig. 3(b) and (d) for the 1T and 2H phases, respectively. The Helmholtz free energy decreases steadily as temperature increases, and it becomes negative at approximately $T \approx 350$ K for both monolayers. This trend indicates that thermal contributions help freestanding monolayers remain stable at moderate temperatures. This means they can be produced under conditions that can be tested in the laboratory.

The entropy $S(T)$ increases steadily with temperature. This is because phonon modes become more active, thereby increasing disorder in lattice vibrations. This behavior is consistent with observations in other stable two-dimensional materials, such as transition-metal dichalcogenides and oxide-based MXene analogues. It also supports the idea that the lattice dynamics in Y_2TeO_2 monolayers are strong.

The temperature dependence of the heat capacity, $C_v(T)$, provides additional information about how the system vibrates. At low temperatures ($T < 300$ K), C_v exhibits a T^3 dependence consistent with the Debye model and the third law of thermodynamics, indicating that only long-wavelength acoustic phonons significantly influence the thermal response. At elevated temperatures ($T > 300$ K), C_v progressively saturates, converging towards the classical Dulong–Petit limit ($C_v = 3R$) [47]. This saturation happens at about $100 \text{ J K}^{-1} \text{ mol}^{-1}$ for both the 1T and 2H phases. This means that all phonon modes are fully excited. The fact that the C_v curves for the two polymorphs are so similar shows that changes in stacking sequence only have a small effect on their overall vibrational thermodynamics.

To further validate the structural stability of the Y_2TeO_2 monolayers, their mechanical stability was examined according to the Born–Huang criteria for hexagonal 2D systems [48]. These criteria say that the elastic constant C_{11} must be positive ($C_{11} > 0$) and bigger than C_{12} ($C_{11} > C_{12}$). Both the 1T and 2H phases meet these requirements. The in-plane elastic stiffness tensor C_{ij} can be expressed as

$$C_{ij} = \begin{pmatrix} C_{11} & C_{12} & 0 \\ C_{12} & C_{11} & 0 \\ 0 & 0 & C_{66} = \frac{C_{11}-C_{12}}{2} \end{pmatrix}, \quad (2)$$

where symmetry relations impose $C_{11} = C_{22}$ and $C_{12} = C_{21}$. The calculated elastic constants for the Y_2TeO_2 -1T monolayer are $C_{11} = C_{22} = 139.52 \text{ N/m}$, $C_{12} = 38.63 \text{ N/m}$, and $C_{66} = 51.68 \text{ N/m}$. For the Y_2TeO_2 -2H phase, the corresponding values are $C_{11} = C_{22} = 147.36 \text{ N/m}$, $C_{12} = 48.51 \text{ N/m}$, and $C_{66} = 41.42 \text{ N/m}$. These values clearly fulfill the Born–Huang stability conditions [48], confirming the mechanical robustness of both polymorphs.

Using the elastic constants, we further investigated the directional dependence of the in-plane mechanical properties, namely the Young’s modulus $Y(\theta)$, shear modulus $G(\theta)$, and Poisson’s ratio $\nu(\theta)$, as functions of the in-plane angle $\theta \in [0, 2\pi]$. The corresponding angular variations are presented in Fig. 4(a)–(c) and were obtained from Eqs. (3)–(4)–(5).

$$Y(\theta) = \frac{C_{11}C_{22} - C_{12}^2}{C_{11}s^4 + C_{22}c^4 + \left(\frac{C_{11}C_{22} - C_{12}^2}{C_{66}} - 2C_{12}\right)c^2s^2}, \quad (3)$$

$$G(\theta) = \frac{C_{66}}{1 + \left(C_{66} \frac{C_{11} + C_{22} + 2C_{12}}{C_{11}C_{22} - C_{12}^2} - 3\right)c^2s^2} \quad (4)$$

and,

$$\nu(\theta) = \frac{C_{12}(s^4 + c^4) - \left(C_{11} + C_{12} - \frac{C_{11}C_{22} - C_{12}^2}{C_{66}}\right)c^2s^2}{C_{11}s^4 + C_{22}c^4 + \left(\frac{C_{11}C_{22} - C_{12}^2}{C_{66}} - 2C_{12}\right)c^2s^2}, \quad (5)$$

where $s = \sin(\theta)$ and $c = \cos(\theta)$.

The polar plots reveal that $Y(\theta)$, $G(\theta)$, and $\nu(\theta)$ exhibit an almost isotropic angular dependence for both the 1T and 2H monolayers, consistent with their underlying hexagonal symmetry. Only minor deviations from perfect circularity are observed, which can be attributed to subtle differences in atomic stacking and bonding environments between the two phases.

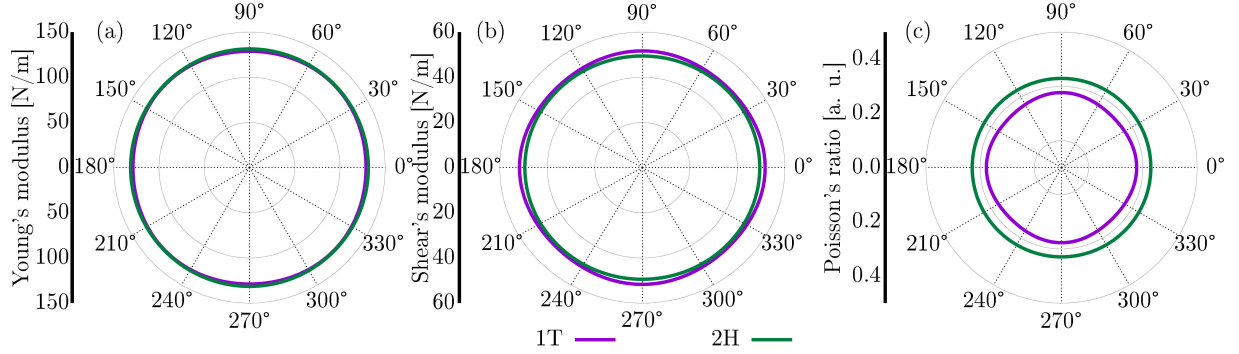


Figure 4: Polar plots of the in-plane mechanical properties of the Y_2TeO_2 monolayers: (a) Young’s modulus $Y(\theta)$, (b) shear modulus $G(\theta)$, and (c) Poisson’s ratio $\nu(\theta)$ for the 1T and 2H phases. The nearly isotropic angular dependence reflects the hexagonal symmetry and mechanical robustness of both structures.

Quantitatively, the maximum Young’s modulus of the Y_2TeO_2 -1T phase reaches $Y_{\max} = 130.39$ N/m, with a corresponding maximum shear modulus of $G_{\max} = 51.68$ N/m and a maximum Poisson’s ratio of $\nu_{\max} = 0.28$. For the Y_2TeO_2 -2H monolayer, the in-plane stiffness is slightly higher, with $Y_{\max} = 131.39$ N/m, while $G_{\max} = 49.43$ N/m and $\nu_{\max} = 0.33$. These values indicate that both polymorphs combine moderate in-plane stiffness with mechanical flexibility.

When compared to other two-dimensional materials, the Young’s moduli of Y_2TeO_2 monolayers are lower than that of graphene (~ 340 N/m), but are comparable to or exceed those of many transition-metal dichalcogenides, such as MoS_2 (~ 120 N/m), and several functionalized MXenes. This balance between stiffness and isotropy is particularly advantageous for applications in flexible optoelectronic and photovoltaic devices, where mechanical integrity under strain is a critical requirement.

3.2 Electronic properties

Figure 5(a) and (c) show the electronic band structures of the Y_2TeO_2 monolayers in the 1T and 2H phases, respectively. At the PBE level, both monolayers have a direct band gap at the Γ point. The gap value for Y_2TeO_2 -1T is 0.84 eV and the gap value for Y_2TeO_2 -2H is 0.89 eV. The direct nature of the gap is especially useful for optoelectronic applications because it makes light absorption and radiative recombination more efficient without the need for phonon-assisted transitions.

It is well known that semilocal exchange–correlation functionals such as PBE tend to underestimate band gaps due to self-interaction errors and the absence of nonlocal exchange effects, which result in an overdelocalization of electronic states. To obtain more reliable electronic gaps, we therefore employed the screened hybrid HSE06 functional. As shown in Fig. 5, the inclusion of a fraction of exact Hartree–Fock exchange leads to a significant opening of the band gap, yielding values of 1.42 eV for the 1T phase and 1.47 eV for the 2H phase, while preserving the direct-gap character at the Γ point. These HSE06 band gaps fall within the optimal range for single-junction photovoltaic absorbers according to the Shockley–Queisser criterion and are comparable to those of widely studied two-dimensional semiconductors, such as monolayer MoS_2 (1.6–1.9 eV) and WS_2 [49, 50]. Compared to most functionalized MXenes, which are typically metallic or exhibit very small gaps, the intrinsic semiconducting behavior of Y_2TeO_2 monolayers represents a significant advantage for optoelectronic and energy-harvesting applications.

Figure 5(b) and (d) show the total and projected density of states (TDOS and PDOS) for the Y_2TeO_2 -1T and Y_2TeO_2 -2H monolayers. The PDOS analysis shows that the conduction band minimum is primarily composed of Y d states, with a small contribution from O p orbitals. This indicates that metal and oxygen states are mixing. The valence band maximum, by contrast, arises primarily from O p orbitals, with smaller contributions from Y d and Te p states. This

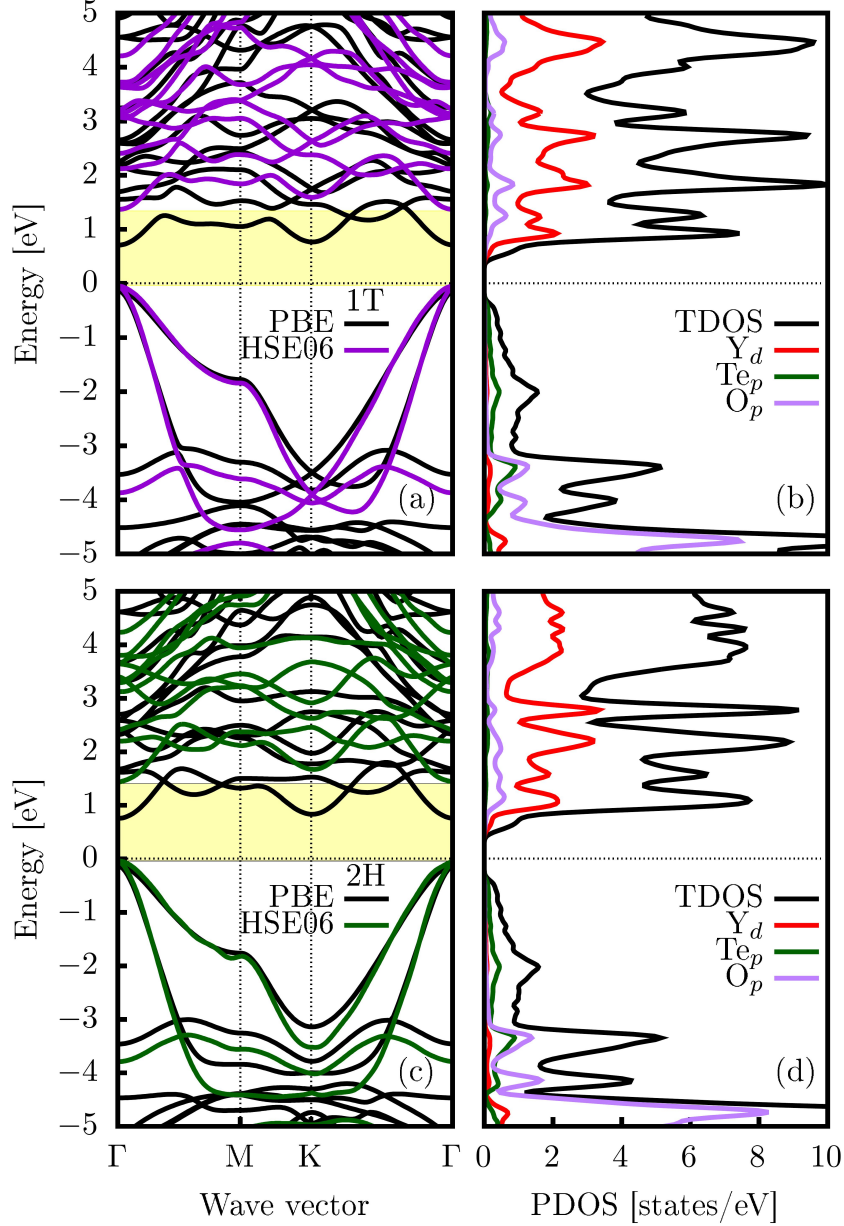


Figure 5: Electronic band structures and density of states of the Y_2TeO_2 monolayers. Panels (a) and (c) show the electronic band structures of the Y_2TeO_2 -1T and Y_2TeO_2 -2H phases, respectively, calculated at the PBE level (black lines) and with the HSE06 hybrid functional (colored lines). Panels (b) and (d) display the corresponding total density of states (TDOS) and projected density of states (PDOS), decomposed into contributions from Y d , Te p , and O p orbitals. The Fermi level is set to zero energy.

orbital distribution clarifies the origin of the direct band gap and highlights the metal–oxygen framework as the key factor governing the electronic structure of Y_2TeO_2 MOenes. The dominant Y d character near the conduction band edge suggests relatively low electron effective masses, which is beneficial for charge transport, while the O p -dominated valence band is expected to support strong light–matter interactions. Similar orbital features have been reported for other metal–oxide-based two-dimensional systems, further reinforcing the consistency of our results with the broader class of MOene materials.

3.3 Excitonic and optical properties

The excitonic properties of the Y_2TeO_2 monolayers were investigated by analyzing the exciton band structures obtained within the MLWF-TB+BSE framework, as shown in Fig. 6(a) and (b) for the 1T and 2H phases, respectively. Although both monolayers exhibit a direct electronic band gap at the Γ point, their exciton ground states are found to be indirect in momentum space. Specifically, the lowest-energy excitons are located near the Γ -M region, with excitation energies of 1.26 eV for Y_2TeO_2 -1T and 1.31 eV for Y_2TeO_2 -2H.

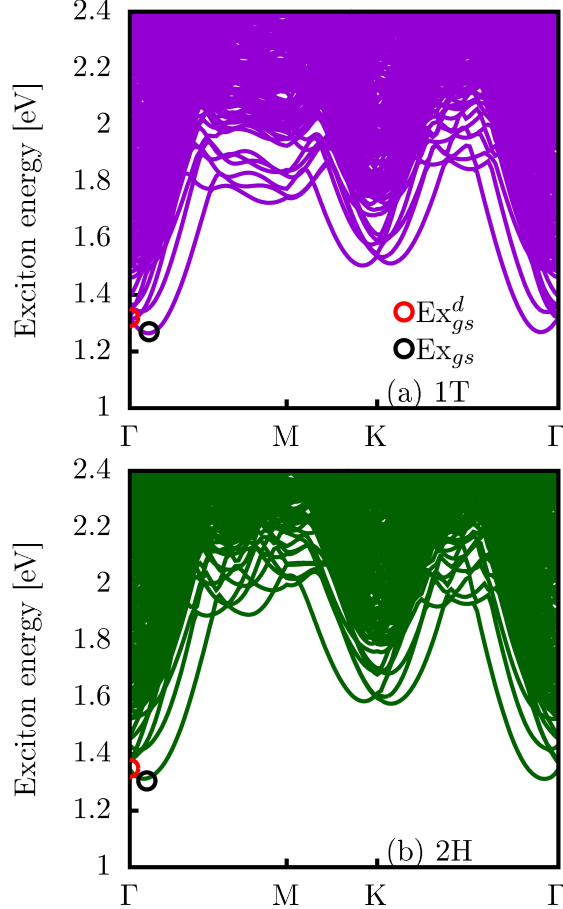


Figure 6: Exciton band structures of the Y_2TeO_2 monolayers obtained from the MLWF-TB+BSE approach. Panels (a) and (b) correspond to the Y_2TeO_2 -1T and Y_2TeO_2 -2H phases, respectively. The lowest-energy indirect exciton ground states (Ex_{gs}) and the direct excitonic states at the Γ point (Ex_{gs}^d) are highlighted.

The exciton ground state is indirect because the excitonic bands spread out, which is a result of the interaction between the electronic band structure and electron-hole interactions. This behavior has also been observed in other 2D semiconductors [51, 52], where excitonic effects can alter the optical response in relation to the underlying electronic gap. As a result, phonon-assisted optical transitions with energies below the direct optical gap can occur, which may affect the absorption onset and radiative recombination processes.

The exciton binding energies, which are shown in Table 2, were found by taking the difference between the fundamental electronic band gap and the exciton ground-state energy. The binding energies calculated are 152 meV for the 1T phase and 126 meV for the 2H phase, which means that the excitons are moderately bound. These numbers are much higher than what is usually seen in bulk semiconductors, but they are lower than the binding energies that have been seen in strongly confined two-dimensional systems like monolayer transition-metal dichalcogenides, where values over

300 meV are common. This intermediate regime shows a balance between lower dimensionality and better dielectric screening in Y_2TeO_2 MOenes.

Table 2: Excitonic properties of the Y_2TeO_2 monolayers obtained using the MLWF-TB+BSE method with HSE06 parametrization. The table lists the fundamental electronic band gap (E_g), direct band gap (E_g^d), exciton ground-state energy (Ex_{gs}), direct exciton ground-state energy (Ex_{gs}^d), and the exciton binding energy ($\text{Ex}_b = E_g - \text{Ex}_{gs}$) for the 1T and 2H phases.

Parameter	Y_2TeO_2 -1T	Y_2TeO_2 -2H
E_g PBE (eV)	0.84	0.89
E_g HSE06 (eV)	1.42	1.47
E_g^d (eV)	1.42	1.47
Ex_{gs} (eV)	1.26	1.31
Ex_{gs}^d (eV)	1.32	1.35
Ex_b (meV)	152	126

We found direct excitonic transitions at the Γ point, with energies of 1.32 eV for Y_2TeO_2 -1T and 1.35 eV for Y_2TeO_2 -2H. The direct exciton binding energies are equal to the indirect ground state binding energies. This further demonstrates that the interactions between electrons and holes are the primary influence on the low-energy optical response. The fact that the direct exciton energies are close to the best spectral range for absorbing visible and near-infrared light shows how useful Y_2TeO_2 monolayers are for optoelectronic and photovoltaic applications.

Figure 7 shows the optical response of the Y_2TeO_2 -1T and Y_2TeO_2 -2H monolayers. This includes the absorption coefficient $\alpha(\omega)$, reflectivity $R(\omega)$, and refractive index $\eta(\omega)$, which were calculated using both the independent-particle approximation (IPA) and the Bethe–Salpeter equation (BSE) formalism. The optical spectra were analyzed for in-plane light polarizations along the \hat{x} and \hat{y} directions, facilitating the evaluation of potential in-plane anisotropy.

Figure 7(a) and (d) show the absorption spectra. They show that both monolayers absorb a lot of light in the visible and ultraviolet (UV) regions. The Y_2TeO_2 -2H phase shows an almost isotropic absorption response at the IPA level (dashed curves), while the 1T phase shows a polarization dependence that is a little stronger. When the BSE formalism is used to explicitly include excitonic effects (solid curves), both polymorphs show a systematic red shift of the absorption onset. This is because bound electron-hole pairs are forming. This red shift caused by excitons is a typical property of two-dimensional semiconductors. It shows how important many-body effects are for accurately describing their optical properties.

Even though both structures have a hexagonal symmetry, the presence of excitonic effects causes a weak optical anisotropy, as shown by the small differences between the \hat{x} and \hat{y} polarized responses. The absorption spectra in the two in-plane directions are very similar, which means that both Y_2TeO_2 monolayers can be thought of as quasi-isotropic optical absorbers. The existence of significant absorption peaks in the visible spectrum reinforces their suitability for optoelectronic and photovoltaic applications.

The reflectivity spectra shown in Fig. 7(b) and (e) show the same patterns at both the IPA and BSE levels. The reflectivity generally rises with the energy of the photons, peaking in the UV range. At the BSE level, the Y_2TeO_2 -1T monolayer has a maximum reflectivity of about 15.8%, and at the IPA level, it has a maximum reflectivity of about 14.3%. The Y_2TeO_2 -2H phase, on the other hand, has a maximum reflectivity of about 16.2% (BSE) and 17.0% (IPA) for \hat{x} polarization. These moderate reflectivity values are good for light-harvesting applications because they mean that less light is lost when it reflects.

Figures 7(c) and (f) show the refractive index $\eta(\omega)$ that was found using the IPA and BSE methods. The main peaks in the refractive index for the Y_2TeO_2 -1T monolayer are in the visible and near-UV ranges, around 2.42 eV and 3.16 eV at the BSE level. In the \hat{x} direction, η ranges from 1.35 to 2.15 (1.55 to 2.00 at the IPA level). In the \hat{y} direction, it ranges

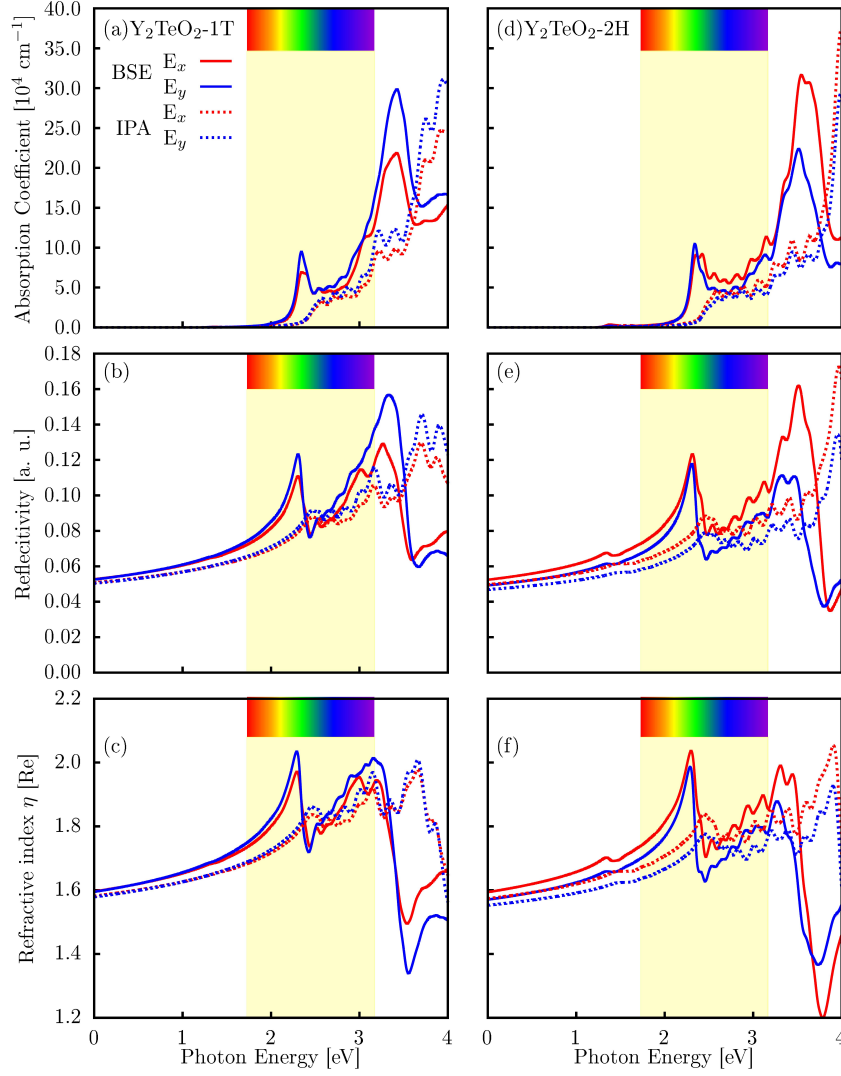


Figure 7: Optical properties of the Y_2TeO_2 monolayers calculated within the independent-particle approximation (IPA) and the Bethe–Salpeter equation (BSE) framework. Panels (a) and (d) show the absorption coefficient $\alpha(\omega)$, panels (b) and (e) the reflectivity $R(\omega)$, and panels (c) and (f) the refractive index $\eta(\omega)$ for the Y_2TeO_2 -1T and Y_2TeO_2 -2H phases, respectively. Solid and dashed curves correspond to BSE and IPA results, while blue and red lines denote light polarized along the \hat{x} and \hat{y} directions. The shaded region highlights the visible spectral range.

from 1.50 to 1.95 (1.55 to 2.02 at the IPA level). The refractive index for the Y_2TeO_2 -2H monolayer is between 1.20 and 2.05 (1.58 and 2.06 at the IPA level) along \hat{x} and between 1.37 and 1.98 (1.56 and 1.90 at the IPA level) along \hat{y} .

3.4 Power conversion efficiency (PCE)

The optical properties discussed above show that Y_2TeO_2 monolayers have strong visible-light absorption and band gaps that are close to the best range for photovoltaic applications. To quantitatively evaluate their efficacy as solar absorbers, we calculated the power conversion efficiency (PCE) employing both the spectroscopic limited maximum efficiency (SLME) framework [53] and the SQ detailed-balance limit [54]. These methods enable a coherent assessment of the interactions among photon absorption, radiative recombination, and electronic band-gap properties, accounting for optical responses at both the independent-particle approximation (IPA) and the Bethe–Salpeter equation (BSE) levels.

The PCE is defined as

$$\text{PCE} = \frac{J_{\text{SC}} V_{\text{OC}} \text{FF}}{P_{\text{SOLAR}}}, \quad (6)$$

where J_{SC} is the short-circuit current density, V_{OC} the open-circuit voltage, FF the fill factor, and P_{SOLAR} the total incident solar power per unit area. The short-circuit current density is obtained from

$$J_{\text{SC}} = \int_{E_g^d}^{\infty} \frac{P(E)}{E} dE, \quad (7)$$

while the total solar power is given by

$$P_{\text{SOLAR}} = \int_0^{\infty} P(E) dE, \quad (8)$$

with $P(E)$ representing the AM1.5G solar spectral irradiance [45, 55].

The current–voltage characteristics of the illuminated solar cell determine the output power density, whose maximum value,

$$P_{\text{PV}} = J(V_{\text{max}}) V_{\text{max}}, \quad (9)$$

is obtained at the operating voltage V_{max} . The current density $J(V)$ is expressed as

$$J(V) = J_{\text{SC}} - \frac{J_0}{f_r} \left[\exp\left(\frac{eV}{k_{\text{B}}T}\right) - 1 \right], \quad (10)$$

where J_0 is the reverse saturation current density, f_r the radiative recombination fraction, e the elementary charge, k_{B} the Boltzmann constant, and T the device temperature.

Within the SLME framework, the photogenerated current density is evaluated as

$$J_{\text{SC}} = e \int_0^{\infty} a(E) \frac{P(E)}{E} dE, \quad (11)$$

where $a(E)$ is the absorbance. The reverse saturation current density is determined from detailed balance under thermal equilibrium,

$$J_0 = e\pi \int_0^{\infty} a(E) \Phi_{\text{bb}}(E) dE, \quad (12)$$

with the blackbody photon flux given by

$$\Phi_{\text{bb}}(E) = \frac{2E^2}{h^3 c^2} \left[\exp\left(\frac{E}{k_{\text{B}}T}\right) - 1 \right]^{-1}. \quad (13)$$

In Table 3, you can see a summary of the PCE values we got for the Y_2TeO_2 monolayers in the 1T and 2H phases at both the IPA and BSE optical levels. The SLME efficiencies calculated using the realistic absorbance of freestanding monolayers are under 0.3%. This is because two-dimensional materials are only a few atoms thick, which makes it very hard for light to be absorbed. Other pristine 2D absorbers have also been found to have low efficiencies, underscoring the difficulty of using isolated monolayers directly in photovoltaic devices.

Prior research has shown that light-trapping techniques, optical cavities, and multilayer stacking can significantly increase the effective absorbance of two-dimensional materials, potentially nearing unity [59]. These results led us to look into the highest possible SLME ($\text{PCE}_{\text{max}}^{\text{SLME}}$), assuming that all photons with energies above the direct band gap are absorbed perfectly. In this idealized situation, the Y_2TeO_2 -1T monolayer has a maximum PCE of 32.27% (IPA) and 30.56% (BSE), while the Y_2TeO_2 -2H phase has a maximum PCE of 31.55% (IPA) and 31.57% (BSE). These numbers are close to the Shockley–Queisser limit, indicating that Y_2TeO_2 has favorable band-gap alignment for solar energy conversion.

Table 3: Calculated power conversion efficiencies (PCEs) of the Y_2TeO_2 monolayers in the 1T and 2H phases obtained within the SLME and SQ frameworks at $T = 300$ K compared to literature. PCE^{SLME} corresponds to efficiencies calculated using the realistic absorbance of freestanding monolayers at the IPA and BSE optical levels. PCE_{max}^{SLME} denotes the maximum SLME assuming ideal absorption above the direct band gap, while PCE^{SQ} represents the SQ detailed-balance limit.

System	Level	PCE^{SLME}	PCE_{max}^{SLME}	PCE^{SQ}	Ref.
Y_2TeO_2 -1T	IPA	0.16	32.27	32.27	This work
Y_2TeO_2 -1T	BSE	0.28	30.56	32.35	This work
Y_2TeO_2 -2H	IPA	0.15	31.55	31.49	This work
Y_2TeO_2 -2H	BSE	0.29	31.57	32.66	This work
ScNbCO ₂ -1T	IPA	-	14.33	20.20	Ref.[25]
ScNbCO ₂ -1T	BSE	-	20.68	29.27	
ScYC(OH) ₂ -1T	IPA	0.45	29.76	29.76	Ref.[22]
ScYC(OH) ₂ -1T	BSE	0.32	16.82	23.44	
Y_2CCl_2 -1T	IPA	0.93	26.31	27.32	Ref.[56]
Y_2CCl_2 -1T	BSE	0.99	32.67	32.67	
Y_2CBr_2 -1T	IPA	0.61	14.10	19.32	Ref.[56]
Y_2CBr_2 -1T	BSE	1.02	31.73	32.08	
Y_2Cl_2 -1T	IPA	0.95	19.62	29.24	Ref.[56]
Y_2Cl_2 -1T	BSE	1.23	29.85	32.12	
Y_2CH_2 -1T	IPA	0.85	27.14	28.47	Ref.[56]
Y_2CH_2 -1T	BSE	0.79	29.85	32.11	
SiI ₂ -1T	IPA	0.24	6.45	7.84	Ref.[57]
SiI ₂ -1T	BSE	0.54	13.57	16.37	
PdS ₂ -1T	IPA	1.03	16.64	18.26	Ref.[58]
PdS ₂ -1T	BSE	1.28	27.89	28.95	
PdSe ₂ -1T	IPA	1.26	21.19	29.88	Ref.[58]
PdSe ₂ -1T	BSE	1.24	26.45	32.32	

The SQ analysis predicts that single-junction solar cells have the optimal band gap of approximately 1.4 eV [54]. The direct HSE06 band gaps of 1.42 eV for the 1T phase and 1.47 eV for the 2H phase are nearly identical—the SQ efficiencies at the IPA level range from 31.49% to 32.27%. When excitonic effects are included using the BSE formalism, the values increase slightly to 32.35% and 32.66%. This improvement demonstrates how excitonic interactions can alter the optical absorption profile and increase the theoretical upper limits of photovoltaic performance.

Table 3 also presents PCEs of different materials predicted at SLME and SQ levels, which are carefully listed. The proposed Y_2TeO_2 monolayers have an excellent PCE excitonic solar cells compared to the literature. For example, the PCE^{SQ} of the ScNbCO₂-1T phase monolayer at the IPA (BSE) levels are 20.20% (29.27%) [25]. Likewise, ScYC(OH)₂-1T phase showed PCE^{SQ} values of 29.76% (23.44%) [22]. Yttrium MXenes monolayers were reported with values of 19.32% to 29.24% (32.11% to 32.67%) at the IPA (BSE) levels [56], respectively. In addition, silicon diiodide XI₂-1T was reported with PCE^{SQ} of 7.84% (16.37%) at the IPA (BSE) levels [57]. Also, PdS₂-1T and PdSe₂-1T monolayers showed values of 18.26% and 29.88% at IPA level, while 28.95% and 32.32% at the BSE level [58]. Our optimal results suggest that as long as the material has a band gap value between 1.30 eV and 1.40 eV, it will exhibit an excellent response because this is an optimal solar region [54, 59].

It is important to mention that a band gap of 1.42 eV for the 1T phase and 1.47 for the 2H phase is close to the optimum region for solar harvesting. In addition, a good PCE means that the materials have a low exciton binding energy ranging between 126 meV (Y_2TeO_2 -2H) and 152 meV (Y_2TeO_2 -1T), which would facilitate efficient exciton dissociation into free charge carriers [60, 61]. This suggests that Y_2TeO_2 monolayers in 1T and 2H phases achieve efficiencies comparable to or higher than those of other recently proposed 2D monolayers.

4 Conclusions

Herein, we present a systematic first-principles investigation of the structural stability and optoelectronic performance of Y_2TeO_2 MOene monolayers in the 1T and 2H phases. Both polymorphs satisfy the criteria for dynamical and mechanical stability, as confirmed by phonon dispersion, elastic analysis, and exhibit nearly isotropic in-plane elastic behavior with stiffness comparable to other robust 2D nanosystems. These features indicate that Y_2TeO_2 can sustain mechanical integrity under practical device conditions. Electronic structure calculations reveal direct band gaps at the Γ point of 1.42 eV (1T) and 1.47 eV (2H), placing both phases within the optimal range for single-junction photovoltaic absorbers. The similarity in band-gap magnitude across phases suggests structural flexibility without significant compromise in electronic performance.

Many-body analysis further shows that electron-hole interactions lead to moderately bound excitons, with binding energies of 152 meV and 126 meV for the 1T and 2H phases, respectively. These values indicate appreciable Coulomb interaction in the 2D limit while remaining favorable for exciton dissociation under operational conditions. The inclusion of excitonic effects produces a red shift in the optical absorption edge, highlighting the importance of beyond-independent-particle treatments for accurate optical prediction. The optical response demonstrates strong absorption across the visible and ultraviolet regions, moderate reflectivity, and weak in-plane anisotropy, supporting broadband light-harvesting capability. Although an isolated monolayer inherently limits absolute light absorption due to atomic thickness, the calculated spectroscopic limited maximum efficiency and Shockley-Queisser limits reach 33%. This high theoretical efficiency originates from the near-ideal band-gap alignment and favorable absorption characteristics. Thus, our results establish Y_2TeO_2 MOene as a structurally stable, direct-band-gap 2D semiconductor with balanced excitonic and optical properties. When integrated into multilayer stacks, van der Waals heterostructures, and light-management architectures, these monolayers hold strong potential for next-generation optoelectronic and photovoltaic applications.

Acknowledgments

This work was supported by the Brazilian funding agencies Fundação de Amparo à Pesquisa do Estado de São Paulo–FAPESP, grants 2024/21870-8, 2022/16509-9, and 2024/05087-1), and National Council for Scientific, Technological Development–CNPq, grant no. 307213/2021–8. The authors gratefully acknowledge financial support from the following institutions: the National Council for Scientific and Technological Development (CNPq), the Federal District Research Support Foundation (FAPDF), and the Coordination for Improvement of Higher Education Personnel (CAPES). The authors also express their gratitude to the National Laboratory for Scientific Computing for providing resources through the Santos Dumont supercomputer, and to the “Centro Nacional de Processamento de Alto Desempenho em São Paulo” (CENAPAD-SP, UNICAMP/FINEP - MCTI project) for support related to projects 897 and 909. Additional resources were provided by Lobo Carneiro HPC (NACAD) at the Federal University of Rio de Janeiro (UFRJ) for project 133. L.A.R.J acknowledges financial support from FAPDF-PRONEM grant 00193.00001247 /2021-20, PDPG-FAPDF-CAPES Centro-Oeste grant number 00193-00000867/2024-94, and CNPq grants 301577/2025-0 and 444111/2024-7. A.C.D. acknowledges financial support from FAP-DF grants 00193-00001817/2023-43 and 00193-00002073/2023-84, CNPq grants 408144/2022-0, 305174/2023-1, 444069/2024-0, and 444431/2024-1.

References

- [1] Armin Vahid Mohammadi, Johanna Rosen, and Yury Gogotsi. The world of two-dimensional carbides and nitrides (mxenes). *Science*, 372(6547):eabf1581, 2021.
- [2] Bikun Zhang, Jian Zhou, and Zhimei Sun. Mbenes: progress, challenges and future. *Journal of Materials Chemistry A*, 10(30):15865–15880, 2022. ISSN 2050-7496. doi:10.1039/d2ta03482d. URL <http://dx.doi.org/10.1039/D2TA03482D>.

- [3] Babak Anasori and Yury Gogotsi. Introduction to 2d transition metal carbides and nitrides (mxenes). In *2D Metal Carbides and Nitrides (MXenes) Structure, Properties and Applications*, pages 3–12. Springer, 2019.
- [4] Dequan Er, Junwen Li, Michael Naguib, Yury Gogotsi, and Vivek B Shenoy. Ti₃C₂ mxene as a high capacity electrode material for metal (li, na, k, ca) ion batteries. *ACS applied materials & interfaces*, 6(14):11173–11179, 2014.
- [5] Michael Naguib, Michel W Barsoum, and Yury Gogotsi. Ten years of progress in the synthesis and development of mxenes. *Advanced Materials*, 33(39):2103393, 2021.
- [6] Michael Naguib, Olha Mashtalir, Joshua Carle, Volker Presser, Jun Lu, Lars Hultman, Yury Gogotsi, and Michel W. Barsoum. Two-dimensional transition metal carbides. *ACS Nano*, 6(2):1322–1331, 2012. doi:10.1021/nn204153h.
- [7] Onkar Jaywant Kewate and Sathyanarayanan Punniyakoti. The role of hcl/lif concentrations in the minimally intensive layer delamination (mild) approach for synthesis of ti₃c₂tx mxenes. *Results in Engineering*, page 108598, 2025.
- [8] Habiba Kiran, Ali BM Ali, Robina Ashraf, Muhammad Bilal Tahir, Mohammad Nasir, Naveed Hasnain, Muhammad Farhat Ullah, Dilsora Abduvalieva, and Nadia Batool. Comparative study of ti₃c₂tx mxene synthesized via hf and lif-hcl etching: Structural, optical, and photocatalytic insights. *Journal of Inorganic and Organometallic Polymers and Materials*, pages 1–14, 2025.
- [9] Xinyue Zhang, Wu Zhang, and Haitao Zhao. Electrochemical performance of ti₃c₂tx mxenes obtained via ultrasound assisted lif-hcl method. *Materials Today Communications*, 33:104384, 2022. ISSN 2352-4928. doi:https://doi.org/10.1016/j.mtcomm.2022.104384. URL https://www.sciencedirect.com/science/article/pii/S2352492822012259.
- [10] Wei Hu, Mingcong Yang, Tiejian Fan, Zhuangxia Li, Yang Wang, Hengzheng Li, Guang Zhu, Jun Li, Huile Jin, and Lianghao Yu. A simple, efficient, fluorine-free synthesis method of mxene/ti₃c₂tx anode through molten salt etching for sodium-ion batteries. *Battery Energy*, 2(5):20230021, 2023. doi:https://doi.org/10.1002/bte2.20230021.
- [11] Yi Wei, Peng Zhang, Razium A. Soomro, Qizhen Zhu, and Bin Xu. Advances in the synthesis of 2d mxenes. *Advanced Materials*, 33(39):2103148, 2021. doi:https://doi.org/10.1002/adma.202103148.
- [12] Satoshi Kajiyama, Lucie Szabova, Hiroki Inuma, Akira Sugahara, Kazuma Gotoh, Keitaro Sodeyama, Yoshitaka Tateyama, Masashi Okubo, and Atsuo Yamada. Enhanced li-ion accessibility in mxene titanium carbide by steric chloride termination. *Advanced Energy Materials*, 7(9):1601873, 2017.
- [13] Varun Natu and Michel W Barsoum. Mxene surface terminations: a perspective. *The Journal of Physical Chemistry C*, 127(41):20197–20206, 2023.
- [14] Varun Natu, Rahul Pai, Olivia Wilson, Edward Gadasu, Hussein Badr, Avishek Karmakar, Andrew JD Magenau, Vibha Kalra, and Michel W Barsoum. Effect of base/nucleophile treatment on interlayer ion intercalation, surface terminations, and osmotic swelling of ti₃c₂z mxene multilayers. *Chemistry of materials*, 34(2):678–693, 2022.
- [15] Kiana Montazeri, Hussein Badr, Ken Ngo, Kaustubh Sudhakar, Tarek Elmelegy, Joshua Uzarski, Varun Natu, and Michel W Barsoum. Delamination of mxene flakes using simple inorganic bases. *The Journal of Physical Chemistry C*, 127(21):10391–10397, 2023.
- [16] Luo Yan, Jiaojiao Zhu, Bao-Tian Wang, Junjie He, Hai-Zhi Song, Weibin Chu, Sergei Tretiak, and Liujiang Zhou. Two-dimensional moene: From superconductors to direct semiconductors and weyl fermions. *Nano Letters*, 22(13):5592–5599, 2022. doi:10.1021/acs.nanolett.2c01914.
- [17] Joseph Halim, Sankalp Kota, Maria R. Lukatskaya, Michael Naguib, Meng-Qiang Zhao, Eun Ju Moon, Jeremy Pitock, Jagjit Nanda, Steven J. May, Yury Gogotsi, and Michel W. Barsoum. Synthesis and characterization of 2d molybdenum carbide (mxene). *Advanced Functional Materials*, 26(18):3118–3127, 2016. doi:https://doi.org/10.1002/adfm.201505328.

- [18] Babak Anasori, Chenyang Shi, Eun Ju Moon, Yu Xie, Cooper A. Voigt, Paul R. C. Kent, Steven J. May, Simon J. L. Billinge, Michel W. Barsoum, and Yury Gogotsi. Control of electronic properties of 2d carbides (mxenes) by manipulating their transition metal layers. *Nanoscale Horiz.*, 1:227–234, 2016. doi:10.1039/C5NH00125K.
- [19] Syahirah Umairah Mahadi, Siti Nabila Aidit, Norazriena Yusoff, Sharifah Fatmadiana Wan Muhammad Hatta, and Siti Fairus Abdul Sani. Direct functionalization of mo₂ctx mxene via single-step synthesis for printable, flexible, non-invasive moisture detection systems. *Flexible and Printed Electronics*, 10(3):035018, September 2025. ISSN 2058-8585. doi:10.1088/2058-8585/ae03d3. URL <http://dx.doi.org/10.1088/2058-8585/ae03d3>.
- [20] Appala Naidu Gandhi, Husam N Alshareef, and Udo Schwingenschlogl. Thermoelectric performance of the mxenes m₂co₂ (m= ti, zr, or hf). *Chemistry of Materials*, 28(6):1647–1652, 2016.
- [21] Bill D Aparicio-Huacarpuma, Calos M de Oliveira Bastos, José AS Laranjeira, Fábio LL Mendonça, Alysson M Almeida Silva, Julio R. Sambrano, Alexandre Cavalheiro Dias, and Luiz Antonio Ribeiro Junior. Theoretical prediction of 2d y₂cti (t= br, cl, f, h) janus mxene monolayers for photovoltaic applications. *ACS omega*, 10(39):45621–45632, 2025.
- [22] Bill D Aparicio-Huacarpuma, Enesio Marinho Jr, José AS Laranjeira, William F Giozza, Alysson MA Silva, Alexandre C. Dias, and Luiz A Ribeiro Jr. Two-dimensional functionalized mm'₂ct₂ (m= sc; m'= y; t= br, cl, f, h, i, o, oh, s, se, te) mxene monolayers for photovoltaic applications. *The Journal of Physical Chemistry C*, 129(30):13568–13580, 2025.
- [23] Jianhui Yang, Xumeng Zhou, Xuepiao Luo, Shaozheng Zhang, and Liang Chen. Tunable electronic and magnetic properties of cr₂m'₂t₂ (m'≠ti or v; t=o, oh or f). *Applied Physics Letters*, 109(20):203109, 2016. ISSN 0003-6951. doi:10.1063/1.4967983.
- [24] Qingxiao Zhou, Xin Jiang, Weiran Li, Weiwei Ju, Yongliang Yong, and Chengyou Cai. Effect of surface functionalization on the quantum capacitance of m₂cf₂ (m= ti, v, cr, zr, nb, mo) as supercapacitor electrodes. *Materials Today Communications*, 40:110203, 2024.
- [25] Bill D Aparicio-Huacarpuma, José AS Laranjeira, Nicolas F Martins, Fredy M Gonzalo, Kleuton AL Lima, Alysson MA Silva, Julio R Sambrano, and Luiz A Ribeiro Junior. Photovoltaic and gas sensing properties of the novel bimetallic janus nb₂cco₂ mxene. *Surfaces and Interfaces*, page 108135, 2025.
- [26] Bill D Aparicio-Huacarpuma, Marcelo Lopes Pereira Junior, Alysson MA Silva, Alexandre C Dias, and Luiz Antonio Ribeiro Junior. Solar harvesting efficiency of janus m₂ctt' (m= y, sc; t/t'≠ br, cl, f) mxene monolayers for photovoltaic applications. *ACS Applied Energy Materials*, 8(10):6634–6644, 2025.
- [27] Luo Yan, Yiqi Huo, Jiaojiao Zhu, Anqi Huang, Ruiqi Ku, Bao-Tian Wang, Tao Li, and Liujiang Zhou. Thickness-dependent superconductivity and quantum spin hall effects in tin+1on (n= 2, 3) moenes. *Physical Review B*, 110(4), July 2024. ISSN 2469-9969. doi:10.1103/physrevb.110.045421. URL <http://dx.doi.org/10.1103/PhysRevB.110.045421>.
- [28] Luo Yan, Tao Bo, Bao-Tian Wang, Sergei Tretiak, and Liujiang Zhou. Single-layer dititanium oxide ti₂o moene: Multifunctional promises for electride, anode materials, and superconductor. *The Journal of Physical Chemistry Letters*, 12(1):494–500, 2021. doi:10.1021/acs.jpcllett.0c03397.
- [29] Yunjie Fan, Chao Zhang, Xiang Liu, Yue Lin, Guanyin Gao, Chao Ma, Yuewei Yin, and Xiaoguang Li. Structure and transport properties of titanium oxide (ti₂o, tio₁, and ti₃o₅) thin films. *Journal of Alloys and Compounds*, 786:607–613, 2019. ISSN 0925-8388. doi:<https://doi.org/10.1016/j.jallcom.2019.01.381>. URL <https://www.sciencedirect.com/science/article/pii/S0925838819304165>.
- [30] Ruxing Wang, Kangli Wang, Hongwei Tao, Wenjie Zhao, Mao Jiang, Jie Yan, and Kai Jiang. Controllable electrolytic formation of ti₂o as an efficient sulfur host in lithium–sulfur (li–s) batteries. *J. Mater. Chem. A*, 8:11224–11232, 2020. doi:10.1039/D0TA01454K.

- [31] Yu-Lu Wan, Qiu Yang, Tian Zhang, Zhao-Yi Zeng, and Xiang-Rong Chen. High thermoelectric performance in Ti_2O_x ($x=f, \text{Cl}$) moene: A first-principles study incorporating electron–phonon coupling. *Journal of Applied Physics*, 135(12):125106, 2024. doi:10.1063/5.0196117.
- [32] Jian Qiu and Jie Liu. A new type of two-dimensional piezoelectric material: Moene based on Ti_2O and its janus structure. *Materials Letters*, 367:136620, 2024. ISSN 0167-577X. doi:https://doi.org/10.1016/j.matlet.2024.136620. URL https://www.sciencedirect.com/science/article/pii/S0167577X24007584.
- [33] E. Bolen and E. Deligoz. Computational study of mechanical stability and phonon properties of mxenes $\text{Mo}_2\text{SCC}_2\text{T}_2$ ($\text{T}=\text{O}$ and F): 2d materials. *Journal of Applied Physics*, 130(6):065102, 2021.
- [34] P. Hohenberg and W. Kohn. Inhomogeneous electron gas. *Physical Review*, 136(3B):B864–B871, November 1964. ISSN 0031-899X. doi:10.1103/physrev.136.b864. URL http://dx.doi.org/10.1103/physrev.136.b864.
- [35] W. Kohn and L. J. Sham. Self-consistent equations including exchange and correlation effects. *Physical Review*, 140(4A):A1133–A1138, November 1965. ISSN 0031-899X. doi:10.1103/physrev.140.a1133. URL http://dx.doi.org/10.1103/physrev.140.a1133.
- [36] G. Kresse and J. Hafner. *Ab initio* molecular dynamics for open-shell transition metals. *Phys. Rev. B*, 48(17):13115–13118, Nov. 1993. ISSN 0163-1829, 1095-3795. doi:10.1103/physrevb.48.13115. URL https://doi.org/10.1103/physrevb.48.13115.
- [37] G. Kresse and J. Furthmüller. Efficient iterative schemes for *Ab Initio* total-energy calculations using a plane-wave basis set. *Phys. Rev. B*, 54(16):11169–11186, Oct. 1996. ISSN 0163-1829, 1095-3795. doi:10.1103/physrevb.54.11169. URL https://doi.org/10.1103/physrevb.54.11169.
- [38] John P. Perdew, Kieron Burke, and Matthias Ernzerhof. Generalized gradient approximation made simple. *Physical Review Letters*, 77(18):3865–3868, October 1996. ISSN 1079-7114. doi:10.1103/physrevlett.77.3865. URL http://dx.doi.org/10.1103/PhysRevLett.77.3865.
- [39] P. E. Blöchl. Projector augmented-wave method. *Physical Review B*, 50(24):17953–17979, December 1994. ISSN 1095-3795. doi:10.1103/physrevb.50.17953. URL http://dx.doi.org/10.1103/PhysRevB.50.17953.
- [40] G. Kresse and D. Joubert. From ultrasoft pseudopotentials to the projector augmented-wave method. *Physical Review B*, 59(3):1758–1775, January 1999. ISSN 1095-3795. doi:10.1103/physrevb.59.1758. URL http://dx.doi.org/10.1103/PhysRevB.59.1758.
- [41] Jochen Heyd, Gustavo E. Scuseria, and Matthias Ernzerhof. Hybrid functionals based on a screened coulomb potential. *The Journal of Chemical Physics*, 118(18):8207–8215, May 2003. ISSN 1089-7690. doi:10.1063/1.1564060. URL http://dx.doi.org/10.1063/1.1564060.
- [42] Aliaksandr V. Kruckau, Oleg A. Vydrov, Artur F. Izmaylov, and Gustavo E. Scuseria. Influence of the exchange screening parameter on the performance of screened hybrid functionals. *The Journal of Chemical Physics*, 125(22), December 2006. ISSN 1089-7690. doi:10.1063/1.2404663. URL http://dx.doi.org/10.1063/1.2404663.
- [43] Atsushi Togo and Isao Tanaka. First principles phonon calculations in materials science. *Scripta Materialia*, 108:1–5, November 2015. doi:10.1016/j.scriptamat.2015.07.021. URL https://doi.org/10.1016/j.scriptamat.2015.07.021.
- [44] Arash A. Mostofi, Jonathan R. Yates, Young-Su Lee, Ivo Souza, David Vanderbilt, and Nicola Marzari. wannier90: A tool for obtaining maximally-localised wannier functions. *Computer Physics Communications*, 178(9):685–699, May 2008. ISSN 0010-4655. doi:10.1016/j.cpc.2007.11.016. URL http://dx.doi.org/10.1016/j.cpc.2007.11.016.
- [45] Alexandre C. Dias, Julian F.R.V. Silveira, and Fanyao Qu. Wantibexos: A wannier based tight binding code for electronic band structure, excitonic and optoelectronic properties of solids. *Computer Physics Communications*, 285:108636, April 2023. ISSN 0010-4655. doi:10.1016/j.cpc.2022.108636. URL http://dx.doi.org/10.1016/j.cpc.2022.108636.

- [46] Carlo A. Rozzi, Daniele Varsano, Andrea Marini, Eberhard K. U. Gross, and Angel Rubio. Exact coulomb cutoff technique for supercell calculations. *Physical Review B*, 73(20):205119, May 2006. ISSN 1550-235X. doi:10.1103/physrevb.73.205119. URL <http://dx.doi.org/10.1103/physrevb.73.205119>.
- [47] N David Mermin and Neil W Ashcroft. Hans bethe’s contributions to solid-state physics. *International Journal of Modern Physics B*, 20(16):2227–2236, 2006. doi:10.1142/s0217979206034716. URL <http://dx.doi.org/10.1142/S0217979206034716>.
- [48] Sten Hastrup, Mikkel Strange, Mohnish Pandey, Thorsten Deilmann, Per S Schmidt, Nicki F Hinsche, Morten N Gjerding, Daniele Torelli, Peter M Larsen, Anders C Riis-Jensen, Jakob Gath, Karsten W Jacobsen, Jens Jørgen Mortensen, Thomas Olsen, and Kristian S Thygesen. The computational 2d materials database: high-throughput modeling and discovery of atomically thin crystals. *2D Materials*, 5(4):042002, September 2018. ISSN 2053-1583. doi:10.1088/2053-1583/aacfc1. URL <http://dx.doi.org/10.1088/2053-1583/aacfc1>.
- [49] Qing Luan, Chuan-Lu Yang, Mei-Shan Wang, and Xiao-Guang Ma. First-principles study on the electronic and optical properties of ws2 and mos2 monolayers. *Chinese Journal of Physics*, 55(5):1930–1937, October 2017. ISSN 0577-9073. doi:10.1016/j.cjph.2017.08.011. URL <http://dx.doi.org/10.1016/j.cjph.2017.08.011>.
- [50] Saju Joseph, Simil Thomas, Jainy Mohan, Anusha Saji Kumar, Sruthi Thulaseedharan Jayasree, Sabu Thomas, and Nandakumar Kalarikkal. Theoretical study on tuning band gap and electronic properties of atomically thin nanostructured mos2/metal cluster heterostructures. *ACS Omega*, 6(10):6623–6628, March 2021. ISSN 2470-1343. doi:10.1021/acsomega.0c05274. URL <http://dx.doi.org/10.1021/acsomega.0c05274>.
- [51] Bill D. Aparicio-Huacarpuma, Carlos M.O. Bastos, C.A. Vilca Huayhua, Alysson M.A. Silva, Leander Michels, Alexandre C. Dias, and Luiz A. Ribeiro Junior. Excitonic and photovoltaic properties of janus sc2c and y2c mxenes from first-principles calculations. *Computational Condensed Matter*, 46:e01213, April 2026. ISSN 2352-2143. doi:10.1016/j.cocom.2026.e01213. URL <http://dx.doi.org/10.1016/j.cocom.2026.e01213>.
- [52] Diana Y. Qiu, Felipe H. da Jornada, and Steven G. Louie. Optical spectrum of mos₂: Many-body effects and diversity of exciton states. *Phys. Rev. Lett.*, 111:216805, 2013.
- [53] Liping Yu and Alex Zunger. Identification of potential photovoltaic absorbers based on first-principles spectroscopic screening of materials. *Physical Review Letters*, 108(6):068701, February 2012. ISSN 1079-7114. doi:10.1103/physrevlett.108.068701. URL <http://dx.doi.org/10.1103/PhysRevLett.108.068701>.
- [54] William Shockley and Hans J. Queisser. Detailed balance limit of efficiency of p-n junction solar cells. *Journal of Applied Physics*, 32(3):510–519, March 1961. ISSN 1089-7550. doi:10.1063/1.1736034. URL <http://dx.doi.org/10.1063/1.1736034>.
- [55] ASTM-G173-03. Standard tables for reference solar spectral irradiances: Direct normal and hemispherical on 37°tilted surface, astm international, west conshohocken, pa (2012), 2012. URL <https://doi.org/10.1520/g0173-03r20>.
- [56] Bill D. Aparicio-Huacarpuma, Marcelo L. Pereira, Mauricio J. Piotrowski, Celso R. C. Rêgo, Diego Guedes-Sobrinho, Luiz A. Ribeiro, and Alexandre C. Dias. Enhanced solar harvesting efficiency in nanostructured mxene monolayers based on scandium and yttrium. *Nanoscale*, 17(21):13298–13310, 2025. ISSN 2040-3372. doi:10.1039/d4nr05505e. URL <http://dx.doi.org/10.1039/D4NR05505E>.
- [57] Bill Darwin Aparicio-Huacarpuma, José Artigas dos Santos Laranjeira, Kleuton Antunes Lopes Lima, Elie Albert Moujaes, Alysson Martins Almeida Silva, Julio Ricardo Sambrano, Alexandre Cavalheiro Dias, and Luiz Antônio Ribeiro Júnior. Optoelectronic and excitonic study of xi 2 (x = si, ge, sn, and pb) monolayers envisaging potential technological applications. *ACS Omega*, November 2025. ISSN 2470-1343. doi:10.1021/acsomega.5c08479. URL <http://dx.doi.org/10.1021/acsomega.5c08479>.

- [58] Elie A. Moujaes and Alexandre C. Dias. On the excitonic effects of the 1t and 1ot phases of pds2, pdse2, and pdsse monolayers. *Journal of Physics and Chemistry of Solids*, 182:111573, November 2023. ISSN 0022-3697. doi:10.1016/j.jpcs.2023.111573. URL <http://dx.doi.org/10.1016/j.jpcs.2023.111573>.
- [59] Deep Jariwala, Artur R. Davoyan, Joeson Wong, and Harry A. Atwater. Van der waals materials for atomically-thin photovoltaics: Promise and outlook. *ACS Photonics*, 4(12):2962–2970, November 2017. ISSN 2330-4022. doi:10.1021/acsphotonics.7b01103. URL <http://dx.doi.org/10.1021/acsphotonics.7b01103>.
- [60] Bill D. Aparicio Huacarpuma, Muhammad Irfan, Carlos A. Vilca Huayhua, Fábio L. Lopes de Mendonça, Carlos M.O. Bastos, Alexandre C. Dias, and Luiz A. Ribeiro. Electronic structure and light-harvesting efficiency of janus xso ($x = \text{sn, ge}$) monolayers. *Physica E: Low-dimensional Systems and Nanostructures*, 177:116453, February 2026. ISSN 1386-9477. doi:10.1016/j.physe.2025.116453. URL <http://dx.doi.org/10.1016/j.physe.2025.116453>.
- [61] Mathieu Massicotte, Fabien Violla, Peter Schmidt, Mark B. Lundeberg, Simone Latini, Sten Hastrup, Mark Danovich, Diana Davydovskaya, Kenji Watanabe, Takashi Taniguchi, Vladimir I. Fal'ko, Kristian S. Thygesen, Thomas G. Pedersen, and Frank H. L. Koppens. Dissociation of two-dimensional excitons in monolayer wse2. *Nature Communications*, 9(1), April 2018. ISSN 2041-1723. doi:10.1038/s41467-018-03864-y. URL <http://dx.doi.org/10.1038/s41467-018-03864-y>.